# *Interplay of Grain Size Dependent Electronic and Ionic Conductivity in Electrochemical Polarization Studies on Sr-Doped LaMnO*



**Citation:** Huber, Tobias M. et al. "Interplay of Grain Size Dependent Electronic and Ionic Conductivity in Electrochemical Polarization Studies on Sr-Doped $LaMnO_3$(LSM) Thin Film Cathodes." Journal of The Electrochemical Society 165, 9 (2018): F702–F709 © 2018 The Author(s)

**As Published:** http://dx.doi.org/10.1149/2.1081809jes

**Publisher:** Electrochemical Society

**Persistent URL:** http://hdl.handle.net/1721.1/117076

**Version:** Final published version: final published article, as it appeared in a journal, conference proceedings, or other formally published context

# Interplay of Grain Size Dependent Electronic and Ionic Conductivity in Electrochemical Polarization Studies on Sr-Doped $LaMnO_3$ (LSM) Thin Film Cathodes

**Tobias M. Huber,[1,2,3,4,5,z] Edvinas Navickas,[5] Kazunari Sasaki,[1,2,6,7,*] Bilge Yildiz,[4,*] Herbert Hutter,[5] Harry Tuller,[2,3,*] and Juergen Fleig[5,**]**

[1]*Next-Generation Fuel Cell Research Center (NEXT-FC), Kyushu University, Nishi-ku, Fukuoka 819-0395, Japan*
[2]*International Institute for Carbon-Neutral Energy Research (WPI-I2CNER), Kyushu University, Nishi-ku, Fukuoka 819-0395, Japan*
[3]*Department of Materials Science and Engineering, Massachusetts Institute of Technology, Cambridge, Massachusetts 02139, USA*
[4]*Lab. for Electrochem. Interfaces, Department of Nuclear Science and Engineering, Massachusetts Institute of Technology, Cambridge, Massachusetts 02139, USA*
[5]*Institute of Chemical Technologies and Analytics, Vienna University of Technology, Vienna A-1060, Austria*
[6]*Department of Mechanical Engineering, Faculty of Engineering, Kyushu University, Nishi-ku, Fukuoka 819-0395, Japan*
[7]*International Research Center for Hydrogen Energy, Kyushu University, Nishi-ku, Fukuoka 819-0395, Japan*

Many efforts are being made to tune perovskite thin film cathodes toward improving their oxygen reduction kinetics and thereby improving overall solid oxide fuel cell performance. One approach is to enhance oxygen diffusion via introduction of larger concentrations of grain boundaries during thin film growth. While such grain boundary engineering has been shown to enhance ionic transport and surface reaction kinetics in some cases, little attention has been paid on its corresponding influence on electronic conductivity. To provide insights into the role of grain boundaries and their contribution to the cathode performance, we have investigated separately the electronic and ionic conductivity of $La_{0.8}Sr_{0.2}MnO_3$ (LSM) thin films by Van-der-Pauw and $^{18}O$ tracer exchange measurements respectively, as well as their combined contributions by electrochemical impedance spectroscopy. All three types of experiments were performed on the same kind of samples with varying LSM microstructure to illustrate the effects of grain boundaries on both electron and ion conduction. Correlations between active electrode area and microstructure-dependent partial conductivities are presented. The findings can also be used for optimizing current collector spacing in thin film solid oxide fuel cells.

 [DOI: 10.1149/2.1081809jes]

Manuscript submitted March 14, 2018; revised manuscript received May 18, 2018. Published June 20, 2018.

Solid oxide fuel cells (SOFC) offer considerably enhanced chemical to electrical energy conversion efficiencies and reduced emissions compared to conventional combustion based systems. The key cell components of SOFC systems, i.e. anode/solid electrolyte/cathode are most commonly composed of nickel/yttria stabilized zirconia (YSZ) cermet, YSZ electrolyte and a mixed conducting cathode. Strontium doped lanthanum manganite (LSM), with the cubic perovskite crystal structure, remains one of the most widely used cathode material for SOFCs due to a combination of high electronic conductivity, good chemical stability and thermal/chemical expansion compatibility with the YSZ electrolyte.[1] However, given its low ionic conductivity, this leads to typical SOFC operation temperatures to be above 800°C, thereby requiring the use of relatively costly interconnect materials while accelerating SOFC degradation rates.[2] As a consequence, there has been increasing interest in alternative cathode formulations that inherently exhibit both high ionic and electronic conductivity – i.e. high mixed ionic electronic conductivity (MIEC) – and thereby superior electrode performance, reflected in reduced area specific resistance (ASR) and overpotentials, at reduced temperatures. A prime example is the related perovskite lanthanum strontium cobaltite $(La,Sr)CoO_{3-\delta}$ (LSC) for which the oxygen deficiency $\delta$ is significant, leading to high oxygen ion conductivity. Unfortunately, LSC readily reacts with YSZ and exhibits a large effective thermal expansion mismatch with YSZ leading to the buildup of potentially destructive stresses.

It has been demonstrated via $^{18}O/^{16}O$ oxygen exchange experiments, followed by secondary ion mass spectrometry (SIMS) concentration profile analysis, that grain boundaries in LSM exhibit orders of magnitude higher oxygen diffusivity and oxygen surface exchange coefficient than the LSM grains.[3–8] Owing to this grain boundary contribution, the bulk path (via grain boundaries), rather than oxygen reduction at triple phase boundary regions, controls the cathode reaction kinetics of LSM thin film microelectrodes (diameter of 200 μm) with columnar grains (grain diameter of ca. 50 nm and thickness of ca. 200 nm), above 700°C.[8,9] By further decreasing the grain size to achieve a higher grain boundary density or by applying a cathodic bias, this bulk path could continue to dominate the oxygen exchange kinetics of thin film electrodes down to even lower temperatures.[5] Fast kinetics in grain boundaries thus introduces the opportunity to increase the effective ionic conductivity and reaction rate coefficients of LSM cathodes by tailoring their microstructure and thereby simultaneously retaining their attractive features such as chemical and thermal-mechanical compatibility, while enabling SOFCs to operate at reduced temperatures.

This work therefore focuses on grain boundary engineering of LSM thin films as a means of optimizing ionic conductivity and oxygen exchange in LSM. It is shown that a change of the grain boundary density does not only influence the ionic properties, but also impacts the electronic conductivity and usually not in a positive manner. In a first step, the electronic grain boundary conductivity of LSM thin films is determined. The resulting increase of the electronic in-plane sheet resistance in thin films may affect the effective electrochemical polarization resistance.[10–12] In a second step, the relevance of this in-plane sheet resistance for thin film electrodes is quantified. The measured electronic and ionic grain boundary properties are used to estimate experimental and geometrical parameters (temperature, grain size, current collector distance), for which a proper analysis of surface polarization resistances of LSM thin films is possible. Finally, we give experimental examples how a reduced in-plane electronic conductivity due to resistive grain boundaries affects impedance spectroscopic studies of micro-patterned thin film electrodes.

*Electrochemical Society Member.
**Electrochemical Society Fellow.
[z]E-mail: tobias.huber@tuwien.ac.at

**Table I. Summary of all samples with film thickness, grain size, preparation temperature and maximum temperature after deposition pre-treatment. Please note: $LSM_{940}$ is deposited at 800°C but was then post-annealed at 940°C (max. temperature).**

| Sample | Deposition temperature | Substrate | Thickness | Grain size | Max temp. |
|---|---|---|---|---|---|
| $LSM_{940}$ | 800°C | YSZ (100) | 680 nm | ca. 60 nm after heat treatment | 940°C |
| $LSM_{800}$ | 800°C | YSZ (100) | 680 nm | 50 nm | 700°C |
| $LSM_{700}$ | 700°C | YSZ (100) | 200 nm | 40 nm | 700°C |
| $LSM_{600}$ | 600°C | YSZ (100) | 200 nm | 30 nm | 650°C |
| $LSM\_S_{600}$ | 600°C | $AL_2O_3$ (0001) | 200 nm | 30 nm | 660°C |
| $LSM_{940,ME}$ | 700°C | YSZ (100) | 120/240 nm | ca. 60 nm after heat treatment | 940°C |

## Experimental

***LSM thin film preparation.***—LSM thin films were prepared by pulsed laser deposition (PLD). The nominally stoichiometric PLD target was produced from $La_{0.8}Sr_{0.2}MnO_3$ (Sigma Aldrich) powder, which was isostatically pressed into pellets and sintered for 12 h at 1200°C in air. The LSM layers were deposited respectively on single crystal substrates of yttria stabilized zirconia - YSZ (100) ($ZrO_2$ with 9.5 mol% $Y_2O_3$), and on sapphire (0001), both of dimensions 10 *x* 10 *x* 0.5 $mm^3$ obtained from CrysTec GmbH, Germany. Deposition was performed in an oxygen atmosphere with $4{\cdot}10^{-2}$ mbar oxygen pressure using a KrF excimer laser with a wavelength of 248 nm and a pulse frequency of 10 Hz. The laser beam energy was set to 400 mJ per pulse and a target-substrate distance of 6 cm was used.

Different film growth temperatures ranging from 600 to about 800°C were employed to vary the columnar grain diameter, with films deposited onto YSZ designated as $LSM_{600}$, $LSM_{700}$ and $LSM_{800}$, respectively. The subscript indicates the approximate deposition temperature. When deposited on sapphire, the designation $LSM\text{-}S_{600}$, was used. The substrate temperature was measured remotely by an IR pyrometer (Heitronics KT-19.99, Germany). The thickness of the polycrystalline LSM layers was controlled by deposition time and later determined by scanning electron microscopy (SEM) (FEI Quanta 200 FEG, Netherlands) and transmission electron microscopy (TEM) (FEI TECNAI-20) from cross-sectional images with values of ∼200 nm obtained for 10 min deposition times (10 Hz). The grain diameters were estimated by two techniques: atomic force microscopy (AFM) (NanoScope V, Bruker Nano) and TEM. Similar samples were used in Refs. 5,8,9,13,14. Data on some samples discussed in a previous study[8] are included here as part of our overall analysis. The LSM film with the largest grains was obtained by deposition at 800°C and post-annealing in air at 940°C; it is denoted $LSM_{940}$ (Table I).

Platinum capping layers (thickness of about 240 nm) were deposited on top of some LSM films via DC magnetron sputtering (MED 020 Coating System, BAL-TEC, Germany) of Pt (99.95% pure, OGUSSA, Austria) at room temperature. Micropatterning of some LSM films and LSM/Pt bilayers was performed by photolithography and subsequent ion beam etching with 2 keV $Ar^+$ ions (incidence perpendicular to the sample surface). Since those LSM layers were also exposed to 940°C, they are denoted $LSM_{940,ME}$.

In this study, the deposition temperature (or the annealing temperature in case of $LSM_{940}$ and $LSM_{940,ME}$) was the only parameter used to vary the microstructure. All other parameters were kept constant during PLD deposition. While many other parameters, such as laser intensity and energy and partial pressure could be changed as well to optimize the microstructure, and thereby the electronic and/or the ionic conductivity, these are beyond the objectives of the present study.

***Electrochemical impedance spectroscopy (EIS).***—Electrochemical characterization of the LSM and LSM/Pt microelectrodes was performed in symmetrically heated micro contact test station (Huber-Scientific, Austria)[15] by means of two point impedance measurements using an Alpha-A High Resolution Dielectric Analyzer (Novocontrol, Germany). Impedance spectra were recorded at temperatures from 560°C to 960°C in the frequency range between $10^6$ and $10^{-3}$ Hz with a resolution of 5 points per frequency decade. Some results of these measurements were already shown in Ref. 9, together with a detailed description regarding the separation between the surface and bulk path of oxygen reduction.

***Van-der-Pauw measurements.***—Van-der-Pauw measurements are a precise way to determine the electronic conductivity of LSM films by eliminating contributions from the contacts.[16,17] Such measurements were performed in a symmetrically heated Van-der-Pauw test station (Huber-Scientific, Austria) placed in a tube furnace using a Keithley 2611A source meter. Four Pt/Ir tips (tip radius ca. 10 μm) were placed in the four corners of the 10 × 10 $mm^2$ LSM film and a type K thermocouple was placed in the vicinity of the thin film to monitor its temperature. Conductivity measurements were carried out in lab air under ambient pressure conditions for sample temperatures between 300°C and 930°C.

***Isotope exchange depth profile (IEDP) experiments.***—Oxygen isotope exchange experiments were performed at temperatures between 570 and 800°C in a gastight quartz isotope exchange chamber (Huber-Scientific, Austria) filled with 200 mbar 97.1% $^{18}O$ oxygen (Campro Scientific, Germany). The isotope exchange took place for periods between 10 and 30 minutes. Following the exchange, samples were quenched, within seconds, to room temperature in $^{18}O$ atmosphere or in ambient air. Further information dealing with similar exchange experiments on Sr-doped $LaCoO_3$ thin films are given in Ref. 18. The resulting $^{18}O$ depth profiles were subsequently investigated by time-of-flight secondary ion mass spectrometry (ToF-SIMS) (ION-TOF GmbH, Germany ToF-SIMS 5). For these SIMS measurements the collimated burst alignment (CBA) mode, with $Bi_3^{++}$ primary ions (25 keV) was used, enabling accurate determination of $^{18}O$ fractions over a broad intensity range.[19,20] Negative secondary ions were analyzed over an area of 30·30 $\mu m^2$, using a raster of 256·256 measurement points. A 1 keV $Cs^+$ ion beam was used to sputter material from a crater of dimensions 300·300 $\mu m^2$ operating at a sputtering ion current of 70 nA. Surface charging was compensated for by an electron flood gun. The depth profiles of the isotope fraction ($f(^{18}O)$) were obtained by normalizing the integrated intensities I of $^{18}O$ and $^{16}O$ according to

$$f(^{18}O) = \frac{I(^{18}O)}{I(^{16}O) + I(^{18}O)}. \quad [1]$$

A more detailed description of the analysis is given in Refs. 5,8.

## Results and Discussion

***In-plane electronic conductivity.***—The effective in-plane electrical conductivity of LSM films $\sigma_{e,eff}$, obtained by the Van-der-Pauw measurements, are shown in Fig. 1. All the measured LSM thin films on YSZ exhibit activation energies between 0.09 eV and 0.12 eV in the temperature range from 300°C to 700°C. This is in good agreement with the activation energy for electronic conductivity in bulk LSM of 0.1 eV reported by Kuo[21] and Tietz[22] and 0.11 eV by Bai.[23] Above approximately 700°C, the conductivity shows a drastic upturn with an effective activation energy of about 0.76 eV for the $LSM_{940}$ film. This activation energy is in good agreement with the value of 0.77 eV

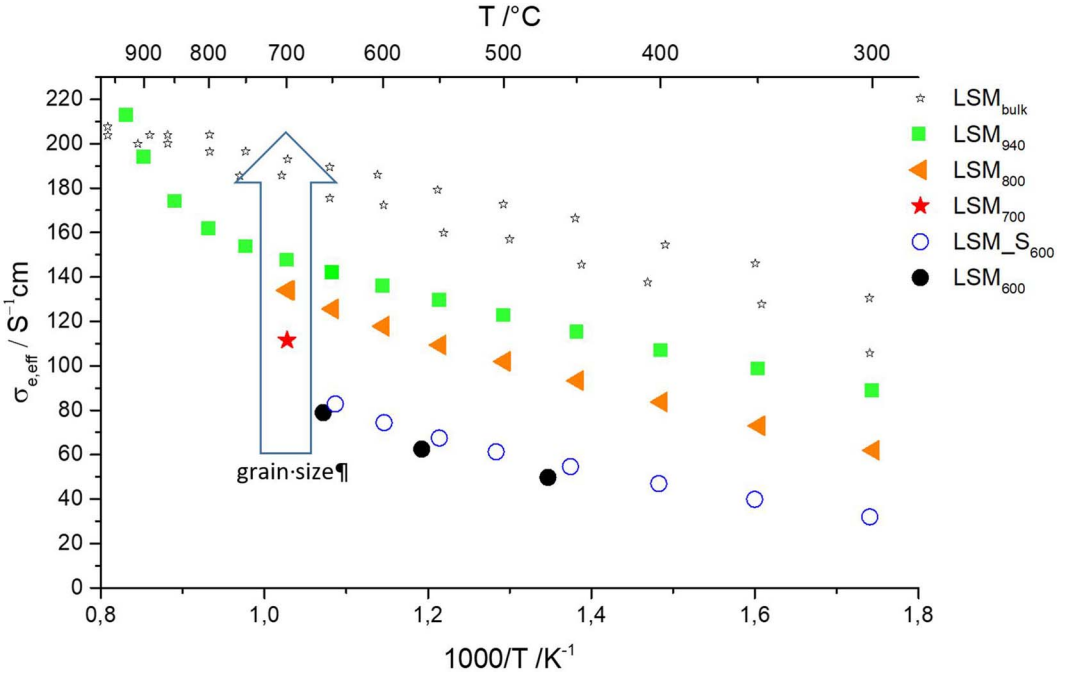


**Figure 1.** Conductivity plot of LSM thin films deposited at different temperatures and measured by the Van der-Pauw technique. Bulk LSM values from Ref. 25 are also included.

reported for ion conduction in similar YSZ single crystal substrates.[24] The strongly increased conductivity values can therefore be attributed to high parallel ionic conductance within the YSZ substrate above 700°C and marks the limit for meaningful electronic in-plane measurements of LSM thin films on YSZ single crystal substrates. Fig. 1 also demonstrates that the measured conductivity of the LSM film on sapphire is in very good agreement with those obtained for LSM films deposited on YSZ at the same temperature (600°C).

Comparison with bulk LSM conductivity at 700°C[25] reveals that all films show lower effective conductivities, see Fig. 1. Moreover, the electronic conductivity clearly scales with the deposition temperature during PLD deposition (Fig. 1) and thereby with the grain size of the LSM film. The higher the deposition temperature, the larger the grain diameter of the columnar LSM grains[5,8] and thereby the higher conductivity. Grain growth can also be attained by post annealing,[9] which further increases the electronic conductivity ($LSM_{940}$ is the $LSM_{800}$ sample after annealing at 940°C). All the data obtained are consistent with the conclusion that grain boundaries hinder in-plane electron transport in LSM and thus lead to effective electronic conductivities lower than LSM bulk conductivity. The LSM films with the smallest grains (ca. 30 nm), for example, exhibit an effective electronic conductivity which is less than 50% of the bulk conductivity.

A first estimate of the specific grain boundary conductivity can be obtained when assuming that the effective conductivity can be described by

$$\frac{1}{\sigma_{e,eff}} = \frac{\delta_{gb}}{\delta_b \sigma_{e,gb}} + \frac{1}{\sigma_{e,b}}. \quad [2]$$

Here, $\sigma_{e,gb}$ and $\sigma_{e,b}$ are the grain boundary and the grain (bulk) conductivity and $\delta_{gb}$, $\delta_b$ are grain boundary thickness and grain size, respectively. Solving for $\sigma_{e,gb}$, one obtains

$$\sigma_{e,gb} = \frac{\delta_{gb}}{\delta_b}\left[\frac{1}{\sigma_{e,eff}} - \frac{1}{\sigma_{e,b}}\right]^{-1}. \quad [3]$$

For an estimated $\delta_{gb} = 2$ nm and a bulk conductivity of 190 S/cm at 700°C,[25] one obtains grain boundary conductivities between 11 and 22 S/cm, see Table II. Grain boundaries thus exhibit about one order of magnitude lower electronic conductivity values than the bulk.

**Table II. Summary of the effective electronic conductivities for all Van-der Pauw measurements at 700°C and the deduced grain boundary conductivities assuming the bulk literature value of 190 S/cm.[25]**

| Sample | Grain size | $\sigma_{e,eff}$ | $\sigma_{e,gb}$ |
|---|---|---|---|
| $LSM_{940}$ | 60 nm | 147 S/cm | 21.7 S/cm |
| $LSM_{800}$ | 50 nm | 134 S/cm | 18.7 S/cm |
| $LSM_{700}$ | 40 nm | 112 S/cm | 13.6 S/cm |
| $LSM_{600}$ | 30 nm | 90 S/cm | 11.4 S/cm |

Very low effective electronic conductivities are reported for LSM thin films by Koep et al., with $\sigma_{e,eff}$ of about 20 S/cm for LSM thin films deposited by PLD at room temperature.[26] This low value might be caused by a very high grain boundary density given that these films were deposited amorphous followed by subsequent annealing to achieve crystallization.

***Across-plane ionic transport.***—The ion conduction $\sigma_i$ was investigated by $^{18}O$ isotope exchange. Diffusion depth profiles were subsequently measured by SIMS (Fig. 2a) and analyzed with a 3D finite-element fitting routine according to Ref. 5 (Fig. 2b). Four individual fitting parameters were obtained, the diffusion coefficients for bulk ($D_b$) and grain boundary ($D_{gb}$) and the surface exchange coefficients for bulk ($k_b$) and grain boundary ($k_{gb}$). From these fitting results, the ionic conductivity of grain and grain boundaries, but also the total area-specific polarization resistance $R_{pol,}$ was calculated using the Nernst–Einstein relation.[27,28] The total polarization resistance consists of two parallel resistive rails, each with an oxygen surface exchange resistance and an ionic transport resistance, one for the grain bulk and one for grain boundaries. Details of these calculations and comparison of these data, obtained by tracer diffusion, with electrochemical impedance data on the same films will be given in a forthcoming paper.

***Comparison of electronic and ionic conductance contributions.***—Generally, when considering the total polarization resistance of LSM electrodes, the focus is on the oxygen exchange

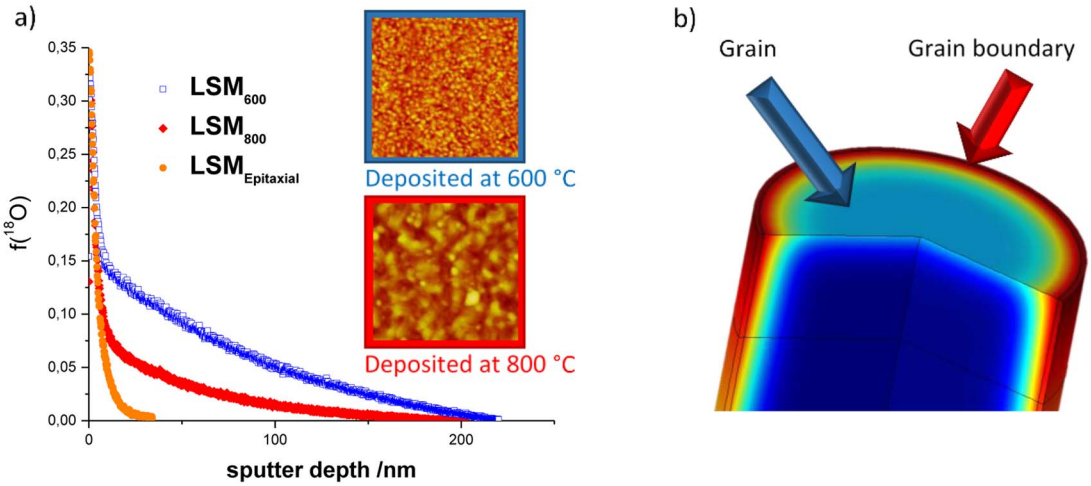


**Figure 2.** a) $^{18}O$ depth profiles obtained by TOF-SIMS of three different micro-structured thin films, exchange was performed at 695°C for 10 minutes in 97.1% $^{18}O$ atmosphere; AFM images of the surfaces are also given. For comparison, a profile for an epitaxial layer without grain boundaries (on $SrTiO_3$) is shown, from Ref. 8. b) Picture of the 3D finite element model used to fit the depth profiles.

or ion transport contributions since the electronic contributions to the overall polarization resistance are often very small, given LSM's highly conductive character ($\sigma_e > 100$ S/cm shown in Fig. 1 vs an ionic contribution of $\sim 10^{-6}$ S/cm at 800°C, both depending on the microstructure). However, with thin films, in-plane sheet resistance contributions become relevant, owing to the very different path lengths covered by the oxygen ions and the electrons. For example, the thin film microelectrodes under EIS study are on the order of 100 nm thick, with lateral dimensions on the order of 100 μm × 100 μm. The cross sectional areas for electrons and ions are respectively 100 μm · 100 nm and 100 μm · 100 μm, while the path lengths are respectively 100 μm and 100 nm. Remembering that the resistance R is the product of the resistivity and the geometrical factor, e.g. path length $d$ divided by the cross sectional area $A$ ($d/A$), one immediately sees that the electrons have a geometrical factor six orders of magnitude greater than that of the ions.

Thus, in considering grain boundary contributions to the measured total electrode polarization resistance, one must be sensitive to ensuring that both the ionic and electronic effective conductivities are affected by grain boundaries. While smaller grain size contributes to faster oxygen exchange at the surface and faster ionic conduction along the grain boundaries, lateral in-plane electronic conductance is hindered by the existence of these same grain boundaries. This asymmetry can be quantified when comparing the electronic sheet resistance $R_{sheet}$, defined by $1/(\sigma_e \cdot d)$ in [Ω] (d = layer thickness), and the nominal area-specific polarization resistance $R_{pol}$ in Ωcm$^2$. $R_{pol}$ includes the oxygen surface exchange resistance and the ion across-plane transport resistance. The in-plane sheet resistance corresponds to the resistance of a square thin film sheet with electrodes at two opposite sides. This pair of resistances gives a good estimate of the situation resulting for current collecting finger electrodes on top or beneath the LSM layer, see sketch in Fig. 3a. The in-plane electronic resistance and the across-plane ionic resistance leads to a transmission line with a polarization decay length λ of[29]

$$\lambda = \sqrt{\frac{R_{pol}}{R_{sheet}}}. \qquad [4]$$

We may thus estimate from the measurement-based grain size dependent $R_{pol}$ and $R_{sheet}$ resistances, for which temperatures and LSM grain sizes the sheet resistance hinders exploiting the entire LSM surface for oxygen reduction. This is illustrated in Fig. 3 for a LSM thin film with finger like current collectors (see sketch in Fig. 3a, finger spacing $w$ of 500 μm) and ionic ($R_{pol}$) as well as electronic ($R_{sheet}$) resistances calculated from our experimental data ($\sigma_{e,eff}$ and tracer fit parameters). For

$$\frac{R_{pol} w^{-2}}{R_{sheet}} = 1, \qquad [5]$$

the decay length equals the finger spacing. Intersecting lines of $R_{pol} w^{-2}$ and $R_{sheet}$ in Fig. 3b thus indicate that the LSM surface is not fully active in oxygen exchange. For a grain size of 30 nm and a current collector distance of 500 μm, this situation is met at ca. 800°C, meaning that narrower current collector spacing is required to fully exploit the better oxygen exchange kinetics of these small-grained LSM films and to determine proper experimental area-specific polarization resistances.

In a further step, we may estimate the critical current collector spacing that is required to benefit from the faster oxygen exchange kinetics of grain boundaries without compromising the overall properties by a decreased in-plane electron conduction. Such a critical distance $w_c$ is estimated by $w_c = \lambda/2$. The resulting values of critical current collector spacing are depicted in Fig. 3c for different temperatures and grain sizes. For example at 700°C and for 30 nm grain size a spacing in the 100 μm range is recommended.

Increasing the film thickness d would strongly improve the situation for electrodes with sole surface exchange limitation (e.g. $LaCoO_3$ based thin film electrodes): The decay length λ in Eq. 4 and thus the active area becomes larger for thicker films, while the area-specific polarization resistance remains constant. Hence, for large current collector spacing the total electrode polarization resistance decreases. However, in thicker LSM layers also the ionic polarization resistance increases due to a longer ion transport path, and thus a thickness increase might have less effect than expected, particularly for rather thick films. In case of pure transport limitation of the ionic path, for example, the decay length in Eq. 4 and thus the active area increases linearly with d, but the area-specific polarization also increases linearly with d and for large current collector spacing the measured (total) electrode polarization resistance is thickness independent.

Another factor that can modify the situation is the electrochemical polarization of LSM thin films by an overpotential. From earlier tracer exchange experiments upon bias voltage it is known that a cathodic voltage improves the bulk ionic conductivity (more oxygen vacancies).[5,13] From partial pressure dependent conductivity measurements[30] one can further predict some decrease of the electronic bulk conductivity for very large cathodic voltages. However, quantitative experimental data do neither exist on the voltage (or chemical potential) dependence of ionic or electronic grain boundary properties nor on the bias dependence of the oxygen surface exchange of LSM thin films. Hence, estimates of proper current collector

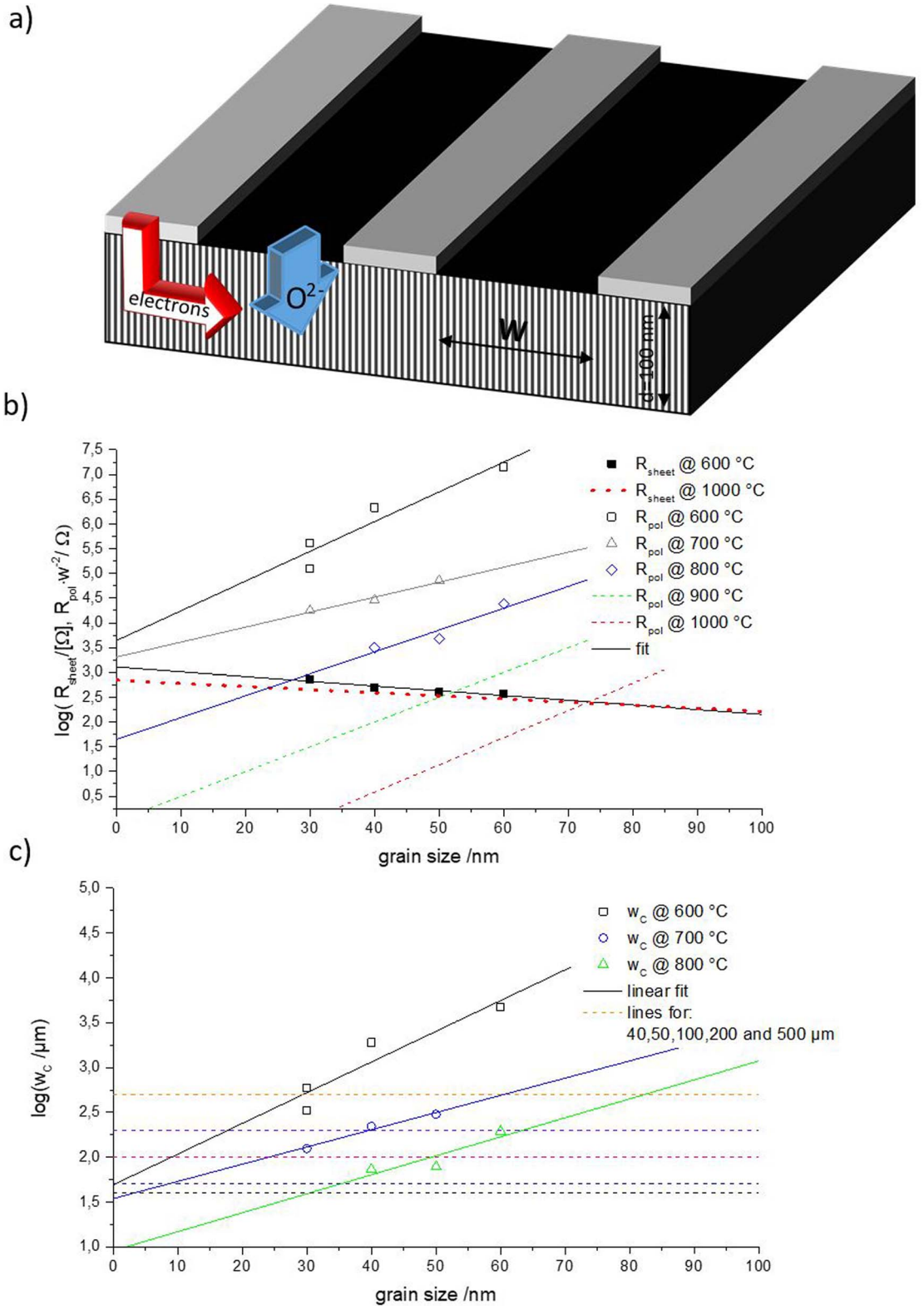


**Figure 3.** a) Sketch of LSM thin film with grain boundaries and current collectors (CC) for probing across-plane ionic oxygen reduction affected by in plane electronic conduction. b) Ionic polarization resistances $R_{pol}$ at 600°C, 700°C and 800°C and extrapolated values at 900°C and 1000°C of 100 nm thin electrodes obtained from the fit values of tracer profiles divided by $w^2$ (for $w = 500\ \mu m$) and sheet resistances, calculated from measured electronic conductivities (extrapolated values for 900 and 1000°C). Intersecting curves indicate that the decay length of the electrochemical polarization equals the current collector spacing w and thus in-plane resistances are certainly relevant. c) Critical current collector distance $w_c$ (defined by $w_c = \lambda/2$) required to avoid a significant decrease of the active surface area for oxygen reduction due to lowered in-plane electronic conduction.

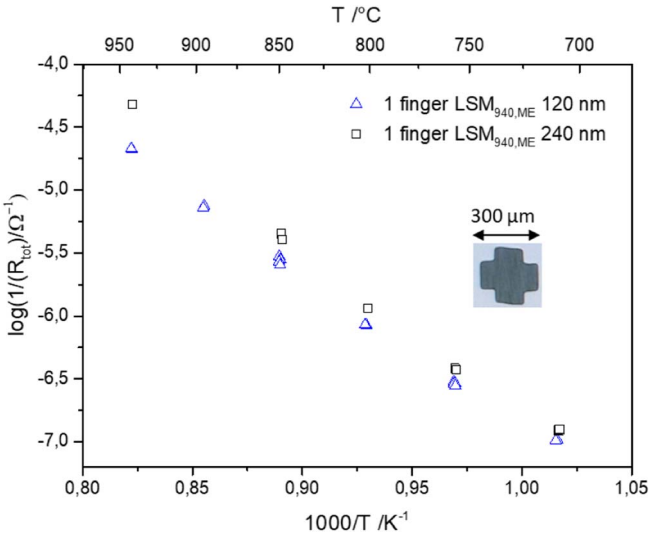


**Figure 4.** Measured inverse electrochemical polarization resistance $R_{tot}^{-1}$ of two $LSM_{940,ME}$ cross-shaped microelectrodes with different thicknesses (120 and 240 nm) with a width of 300 µm.

spacing for measurements upon electrochemical polarization cannot be given yet.

***Consequences for measurements on thin film microelectrodes.—*** The influence of the electronic sheet resistance also becomes clearly visible when carefully examining impedance measurements taken with LSM microelectrodes on YSZ at high temperatures. For electrodes with the same lateral dimensions but varying thickness, the thicker electrode (240 nm) shows a lower total electrode polarization resistance $R_{tot}$ (see Fig. 4), although the thinner electrode (120 nm) should exhibit less resistance due to the shorter oxygen transport path along the LSM grain boundaries. This behavior is due to a decrease of the electrochemically active electrode area in the thinner films, caused by the in-plane electronic resistance. It would be less pronounced if grain boundaries were not highly resistive for electrons. Since the oxygen exchange and transport in grain boundaries is much more thermally activated than the in-plane electronic transport, the importance of this effect increases with temperature. A similar phenomenon, i.e. a limitation of the electrochemically active region by thin current collecting fingers, was also described in Ref. 9.

The electronic in-plane resistance and thus the electron blocking grain boundaries also affect the electrolyte resistance measured in these experiments. This is demonstrated in Fig. 5 by comparing 1-finger and 6-finger electrodes of the same surface area but different spatial extension, see sketch in Fig. 5. For a 6-finger electrode, the current has to be less constricted in the electrolyte and hence one might expect a smaller YSZ bulk resistance due to geometrical reasons. However, from the high frequency intercept of the impedance spectra ($R_{hf}$), which should reflect the electrolyte resistance, the opposite is found, see Fig. 5a, especially at higher temperatures. This indicates that only the inner part of the 6-finger microelectrodes is current carrying at high frequencies, due to a large electronic in-plane resistance in the fingers.

Also for circular microelectrodes the same effect appears. In an additional sample, the electronic sheet resistance of a circular LSM microelectrode (Ø = 290 µm) was short-circuited by applying a platinum capping layer on top. The capped and the uncapped microelectrodes were then contacted by a needle in the center and impedance spectra were measured. At low temperatures the same high frequency intercepts $R_{hf}$ are found. At high temperatures, however, the platinum capped electrode shows a smaller $R_{hf}$ (Fig. 5b). This indicates a decrease of relevant electrode area of the uncapped LSM electrode with increasing temperature and thus an increase of the electrolyte resistance compared to the Pt capped layer.

**Table III. YSZ related high frequency resistances obtained by EIS of 240 nm thick $LSM_{940,ME}$ electrodes with and without Pt layer (see Fig. 5) and the calculated relevant electrode diameter.**

| Measurement temp. | $R_{hf}$ LSM | $R_{hf}$ LSM/Pt | Relevant Ø of LSM (relevant Ø of LSM/Pt) |
|---|---|---|---|
| 700°C | 1550 Ω | 1202 Ω | 224 µm (290 µm) |
| 860°C | 427 Ω | 229 Ω | 156 µm (290 µm) |

To exactly account for the LSM in-plane electronic contribution to $R_{hf}$, a three dimensional variation of a transmission line model would need to be applied. However, such a quantification by combining ionic transport in YSZ and electronic transport in LSM is beyond the scope of this paper. To a first approximation we may simply assume that $R_{hf}$ largely reflects the ionic resistance in YSZ. Then we can use its measured value and the known conductivity ($\sigma_{YSZ}$)-temperature (T) relation ($\sigma_{YSZ} = \sigma^* \cdot \exp(-E_a/kT)$) to estimate the active electrode area, provided the sample is heated symmetrically and the local temperature is known.[15] With parameters $E_a$ and $\sigma^*$, the relevant diameter of the microelectrode area $d_{ME}$ is estimated from Ref. 24

$$\sigma_{YSZ} = \frac{1}{2 d_{ME} R_{hf}}. \quad [6]$$

When short-circuiting the lateral electronic charge transport by addition of a current collecting platinum layer, Fig. 5b, the measured $R_{hf}$ values decrease and correspond to the expected values $R_{YSZ}$ without any electronic LSM in-plane sheet resistance. The estimated relevant diameters $d_{ME}$ in Eq. 6 of the uncapped layers are tabulated in Table III for two temperatures. We see that a $LSM_{940,ME}$ film with grain size ca. 60 nm, 240 nm thickness and Ø = 290 µm shows a nominally active diameter of 224 µm at 700°C and 156 µm at 860°C, respectively. Hence, the relevant area without Pt is reduced by 40% and 71% for 700°C and 860°C, respectively. We can thus conclude from all these additional microelectrode impedance measurements that for a proper analysis it is essential not only to consider possible geometrical dependencies of fast ionic paths along grain boundaries, but also to take into account that electron conduction hindered by grain boundaries affects effective areas and polarization resistances.

## Conclusions

The electronic and ionic conductivities of LSM thin film samples were investigated by Van-der-Pauw measurements and $^{18}O$ tracer exchange experiments. The dependence on grain size, and thus on grain boundary density, could be obtained by varying deposition or annealing temperatures. The electronic in-plane conductivity is decreased by grain boundaries and electronic grain boundary conductivities in the range of 10–20 S/cm at 700°C could be estimated, which is about one order of magnitude lower than the bulk value. The ionic conductivity, as well as the oxygen surface exchange resistance, is improved by grain boundaries. Variation of the thin film microstructure thus induces opposite changes of the across-plane ionic and the in-plane electronic contributions to the overall resistance.

These results were used to determine the relevance of current collector geometries when optimizing the performance of LSM thin film electrodes by grain boundary engineering. An optimal current collector spacing is estimated for different grain sizes and temperatures. For example, a 100 nm thin LSM film of 30 nm grain size should be probed at 700°C with current collector distances not larger than 100 µm, as depicted in Fig. 3c. Moreover, the relevance of a reduced in-plane electronic conductivity due to grain boundaries was shown for resistances derived from electrochemical impedance spectroscopy (EIS) experiments on microelectrodes. This study thus quantitatively reveals the impact of thin film grain boundary engineering on mixed

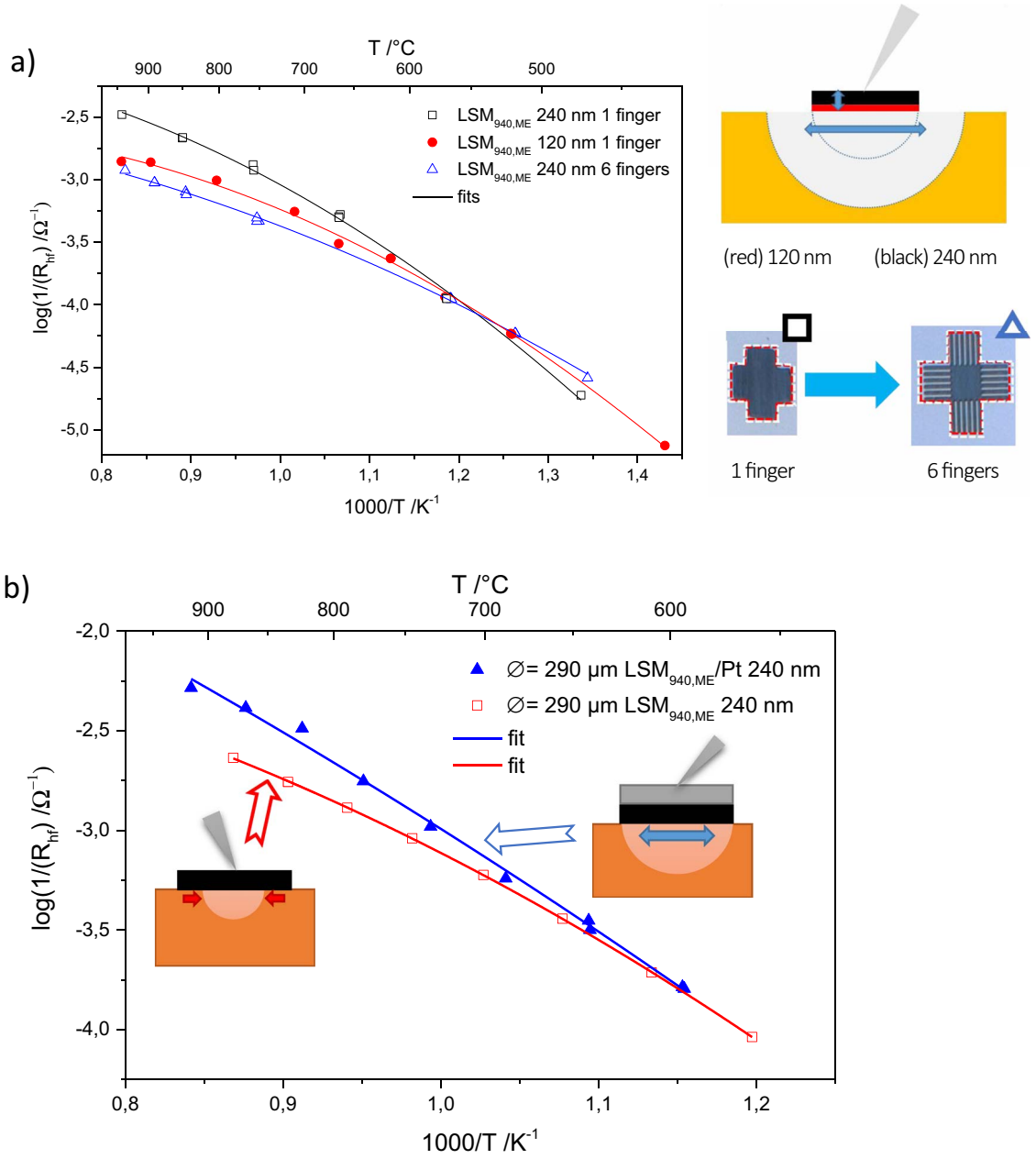


**Figure 5.** a) $R_{hf}$ from $LSM_{940,ME}$ microelectrodes with one and six fingers and film thicknesses of 120 and 240 nm. (Total polarization resistance of the same type of 1 finger electrodes is shown in Fig. 4). b) $R_{hf}$ from two Ø = 290 µm $LSM_{940,ME}$ microelectrodes, one covered with platinum. The sketches indicate the changing volume of YSZ probed by the microelectrodes.

ionic and electronic conductivity and demonstrates the trade-off between lateral electronic sheet and perpendicular oxygen incorporation and transport resistance.

## Acknowledgment

T. M. Huber, K. Sasaki, acknowledge financial support from the Progress-100 program at Kyushu Universitys, E. Navickas and J. Fleig acknowledge support from Austrian Science Fund (FWF) (project: F4509-N16) and the TU Wien University Library for financial support through its Open Access Funding Programme, H.L. Tuller and B. Yildiz acknowledge US-DOE Basic Energy Sciences, grant No. DE-SC0002633 for financial support.

## ORCID

Tobias M. Huber https://orcid.org/0000-0001-6339-8341

## References

1. S. B. Adler, *Chem. Rev.*, **104**, 4791 (2004).
2. N. P. Brandon, D. Corcoran, D. Cummins, A. Duckett, D. Haigh, R. Leah, G. Lewis, N. Maynard, T. Mccolm, and R. Trezona, **13**, 253 (2004).
3. P. S. Lu Yan, Balasubramaniam Kavaipatti, Kee-Chul Chang, and Hoydoo You, *Trans. E C S Soc. Electrochem.*, **35**, 2063 (2011).
4. R. De Souza, J. Kilner, and J. F. Walker, *Mater. Lett.*, **43**, 43 (2000).
5. T. M. Huber, E. Navickas, G. Friedbacher, H. Hutter, and J. Fleig, *ChemElectroChem*, **2**, 1487 (2015).
6. A. M. Saranya, D. Pla, A. Morata, A. Cavallaro, J. Canales-Vázquez, J. A. Kilner, M. M. Burriel, A. Tarancõn, A. Tarancón, A. Tarancõn, A. Tarancón, A. Tarancõn, and A. Tarancón, *Adv. Energy Mater.*, **5**, 0 (2015).

7. R. E. Usiskin, S. Maruyama, C. J. Kucharczyk, I. Takeuchi, and S. M. Haile, *J. Mater. Chem. A*, **00**, 1 (2015).
8. E. Navickas, T. M. Huber, Y. Chen, W. Hetaba, G. Holzlechner, G. M. Rupp, M. Stöger-Pollach, G. Friedbacher, H. Hutter, B. Yildiz, and J. Fleig, *Phys. Chem. Chem. Phys.*, **17**, 7659 (2015).
9. T. M. Huber, M. Kubicek, A. K. Opitz, and J. Fleig, *J. Electrochem. Soc.*, **162**, F229 (2014).
10. D. S. Mebane, Y. Liu, and M. Liu, *J. Electrochem. Soc.*, **154**, A421 (2007).
11. M. E. Lynch, D. S. Mebane, Y. Liu, and M. Liu, *J. Electrochem. Soc.*, **155**, B635 (2008).
12. M. E. Lynch and M. Liu, *J. Power Sources*, **195**, 5155 (2010).
13. T. M. Huber, E. Navickas, K. Sasaki, B. Yildiz, H. Tuller, G. Friedbacher, H. Hutter, and J. Fleig, *J. Electrochem. Soc.*, **164**, F809 (2017).
14. A. K. Opitz, M. Kubicek, S. Huber, T. M. Huber, G. Holzlechner, H. Hutter, and J. Fleig, *J. Mater. Res.*, **28**, 2085 (2013).
15. T. M. Huber, A. K. Opitz, M. Kubicek, H. Hutter, and J. J. Fleig, *Solid State Ionics*, **268**, 82 (2014).
16. L. Yan and P. Salvador, *ACS Appl. Mater. Interfaces*, **4**, 2541 (2012).
17. L. J. Van der Pauw, *Philips Tech. Rev.*, **20**, 220 (1958).
18. M. Kubicek, Z. Cai, W. Ma, B. Yildiz, H. Hutter, and J. Fleig, *ACS Nano*, 3276 (2013).
19. M. Kubicek, G. Holzlechner, A. K. Opitz, S. Larisegger, H. Hutter, and J. Fleig, *Appl. Surf. Sci.*, **289**, 407 (2014).
20. G. Holzlechner, M. Kubicek, H. Hutter, and J. Fleig, *J. Anal. At. Spectrom.*, **28**, 1080 (2013).
21. J. H. Kuo, H. U. Anderson, and D. M. Sparlin, *J. Solid State Chem.*, **87**, 55 (1990).
22. F. Tietz, I. Arul Raj, M. Zahid, and D. Stöver, *Solid State Ionics*, **177**, 1753 (2006).
23. Y. Bai, M. Liu, D. Ding, K. Blinn, W. Qin, J. Liu, and M. Liu, *J. Power Sources*, **205**, 80 (2012).
24. A. K. Opitz and J. Fleig, *Solid State Ionics*, **181**, 684 (2010).
25. J. Mizusaki, *Solid State Ionics*, **132**, 167 (2000).
26. E. Koep, C. Jin, M. Haluska, R. Das, R. Narayan, K. Sandhage, R. Snyder, and M. Liu, *J. Power Sources*, **161**, 250 (2006).
27. J. Maier, *Solid State Ionics*, **112**, 197 (1998).
28. F. S. Baumann, J. Fleig, H.-U. Habermeier, and J. Maier, *Solid State Ionics*, **177**, 1071 (2006).
29. A. Nenning, A. K. Opitz, T. M. Huber, and J. Fleig, *Phys. Chem. Chem. Phys.*, **16**, 22321 (2014).
30. J. Mizusaki, N. Mori, H. Takai, Y. Yonemura, H. Minamiue, H. Tagawa, M. Dokiya, H. Inaba, K. Naraya, T. Sasamoto, and T. Hashimoto, *Solid State Ionics*, **129**, 163 (2000).